Received: 17 July 2019 | Revised: 1 April 2020 | Accepted: 2 April 2020

DOI: 10.1002/cnm.3340

RESEARCH ARTICLE - APPLICATION

WILEY

A novel virtual flow diverter implantation method with realistic deployment mechanics and validated force response

Gábor Závodszky[1,2] | **Benjámin Csippa**[2] | **György Paál**[2] | **István Szikora**[3]

[1]Computational Science Lab, Faculty of Science, Institute for Informatics, University of Amsterdam, Amsterdam, Netherlands

[2]Department of Hydrodynamic Systems, Budapest University of Technology and Economics, Budapest, Hungary

[3]Department of Neurointerventions, National Institute of Clinical Neurosciences, Budapest, Hungary

Correspondence
Gábor Závodszky, Computational Science Lab, Faculty of Science, University of Amsterdam, Amsterdam, Netherlands.
Email: g.zavodszky@uva.nl

Funding information
H2020 European Research Council, Grant/Award Number: 675451; Hungarian BME-Biotechnology FIKP, Grant/Award Number: BME FIKP-BIO; Hungarian National Brain Research Program, Grant/Award Number: 2017-1.2.1-NKP-2017-00002

Abstract

Virtual flow diverter deployment techniques underwent significant development during the last couple of years. Each existing technique displays advantageous features, as well as significant limitations. One common drawback is the lack of quantitative validation of the mechanics of the device. In the following work, we present a new spring-mass-based method with validated mechanical responses that combines many of the useful capabilities of previous techniques. The structure of the virtual braids naturally incorporates the axial length changes as a function of the local expansion diameter. The force response of the model was calibrated using the measured response of real FDs. The mechanics of the model allows to replicate the expansion process during deployment, including additional effects such as the push-pull technique that is required for the deployment of braided FDs to achieve full opening and proper wall apposition. Furthermore, it is a computationally highly efficient solution that requires little pre-processing and has a run-time of a few seconds on a general laptop and thus allows for exploratory analyses. The model was applied in a patient-specific geometry, where corresponding accurate control measurements in a 3D-printed model were also available. The analysis shows the effects of FD oversizing and push-pull application on the radial expansion, surface density, and on the wall contact pressure.

KEYWORDS

virtual stenting, intracranial aneurysm, fast virtual deployment

1 | INTRODUCTION

Intracranial aneurysms (IAs) are focal dilatations on the walls of cerebral arteries. They are most often located along the branches of the Circle of Willis. They affect about 3% to 5% of the population; however, the prevalence of ruptures is comparatively low (around 1 in 10 000 per year[1]). Yet, when a rupture does happen, the results can be devastating. The risk of mortality and morbidity during the first year can be as high as 45%.[2-4] A question often arising in medical practice is when to treat an aneurysm.[5] A rupture event can be catastrophic but the treatments themselves also carry

non-negligible risk.[4,6] Therefore, the development of the available treatment methods is of vital importance. One effective treatment for large and giant wide-necked IAs is the implantation of a flow diverter device into the parent artery across the neck of the aneurysm.[7,8]

The planning of the treatment is far from trivial. Although flow diversion is highly effective in preventing recurrence as opposed to aneurysm packing with coils, it is associated with potential complications, such as failure to occlude, in-stent stenosis,[9,10] delayed bleeding,[11,12] or even in-stent thrombosis.[13] Among others, procedural factors impacting the deployment may play an important role as causes of such complications.[14-16] The material properties, diameter, length of the chosen FD, and the deployment technique may all influence the wall apposition of the device, the porosity across the neck, and the force exerted on the vessel wall by the device.[17-21] Subsequently, the device should be carefully chosen, to best match the individual anatomy of the vessel section involved. This would require a tool that is capable of accurately predicting the possible outcomes of various FD deployment scenarios in each particular case. Beside assisting the physician in understanding the expected mechanical behaviour of the device, such a tool can provide essential input for image-based computational fluid dynamics (CFD) simulations, which can predict the hemodynamical effect of the treatment. Using such a tool may significantly reduce the risk of complications and increase the chances of successful aneurysm occlusion by allowing to compare computed predictions of various deployment scenarios. There are commercial tools available that are supposed to visually demonstrate the behaviour of FDs in the specific anatomies providing a guideline for the physician to choose the appropriate device. Unfortunately, to date, the scientific method applied and the validation results for these techniques remain unknown. To guarantee the accuracy and safety of such tools we believe that it is important to build and validate a method that is capable of accurately simulate the mechanical behaviour of FDs including the dynamic process of device opening and the resulting wall apposition, foreshortening, and forces exerted on the vessel wall.

There are existing solutions trying to address these questions; however, they all present significant limitations. The first methods were based on the deformation of a uniform tube along the centreline of the treated vessel section.[22-24] These virtual FD (vFD) techniques typically result in poor wall apposition, and due to the lack of a realistic mechanical representation, their predictive accuracy is questionable. The later versions can roughly be divided in two categories. The first one consists of detailed finite element analysis (FEA) models taking the specific design and mechanical properties of the FD into account.[19,25,26] While these methods are in theory quite accurate, they require a significant effort to do the pre-processing and the computation. This can be a serious drawback for clinical applications with a constrained timeframe or for larger parametric studies and exploratory investigations. The second category consists of simplified models using surrogate surface structures (such as simplex meshes) to increase the computational efficiency of the model while sacrificing some accuracy.[27-29] The comparative study of Bernardini et al[30] indicated that for simple vessel geometries the difference in accuracy between the FEA and simplified methods can be insignificant. Meanwhile Spranger and Ventikos[31] argued that the accuracy of these simplified models can be questioned in highly tortuous or complex geometries. A common shortcoming of the above methods is that several factors that have an influential part in the deployment are neglected. There are developments towards including the most important ones. For instance, Ma et al[32] presented an extended FEA method to include a mechanism that mimics parts of the push-pull technique during implantation. Bouillot et al[33] implemented a mathematical surface deformation model that can represent the local length change of the FD as the function of the local expansion. Currently, however, there is no single model that can accurately predict the FD surface location when using push-pull, the local surface density after the implantation, and the exerted force on the vessel wall (ie, the contact pressure). These are necessary components to fully evaluate a deployment scenario.

In the following, we present a spring-mass-based model that includes the elastic properties of the FD itself, the effect of length contraction as well as the effects of applied push-pull techniques. Technically, it belongs to the group of simplified representation models, thus it maintains a low-computational cost (typical run-time on the scale of seconds) and needs no additional pre-processing. The method is validated by both mechanical tests and by comparison with a high-resolution digital subtraction angiography (DSA) record of a real FD implanted in a 3D printed IA geometry. Finally, the method is applied to investigate the effects of varying the diameter of an FD and the effects of the applied push-pull technique in the validation geometry.

2 | METHODS

Most of currently used FDs are braided wire meshes that have a relatively low opening force compared with other self-expanding stents. Subsequently, the delivery technique of FDs is substantially different from that used for conventional

stents. Instead of simply unsheathing the device by withdrawing its delivery catheter, once the first segment of the device started opening, these devices need to be pushed by the delivery wire and the catheter should be allowed to be moved back by the slowly opening stent. This technique is often referred to as the push-pull method. Using this technique the operator is capable of significantly influencing the final configuration of the implanted device. More pushing will result in denser wire mesh, better wall apposition and shorter final length, while more unsheathing may stretch the stent resulting in loose mesh density and imperfect wall apposition. In the current work, FDs are represented with an interconnected set of linear springs. The connectivity of the network is motivated by the braided structure of real FDs. The mechanical properties are modelled through two different spring types with differing spring coefficients. One represents the surface mechanics, for example, length contraction (see Figure 1A), while the other one is placed in a radial direction to model the expansion (see Figure 1B). The basic repeating units of this second inner string structure are 'rings' along axial cross-sections. The surface of the vFD is created by connecting these rings with the first spring type in a scissor-like structure.

The linear coefficient of these surface springs are significantly higher than that of the radial springs. This ensures that the virtual braids (ie, the surface springs) have little or no deformation at the end of the simulated deployment; thus, they can represent the quasi-incompressible braids accurately. This structure can be used to model the behaviour of multiple FD types through changing the spring coefficients. In the current work, we set and validate our model according to the behaviour of pipeline embolization device. The scissor-like surface connectivity of springs in the model produces length contraction as a function of radial expansion (shown in Figure 1A) that is fit to the data provided by the vendor. This fitting happens through setting the ratio of dL/dR, which is the connectivity distance to the circumferential distance of the springs making up the virtual braids. The result of this fitting is shown in Figure 2, and Table 1 shows the fitted ratio values.

All the nodes (ie, the endpoints of springs) carry continuous surface coordinates (identically to UV coordinates[34]) from the expanded equilibrium shape. The geometry description of the real FD can be attached to these coordinates to deform it together with the virtual FD similarly to the solution in Reference [27].

The motion of the nodes follow simple Newtonian mechanics:

$$\ddot{x}_i = \frac{F_i}{m}, \tag{1}$$

where x_i is the spatial position of the ith node, m is a fictitious mass, and F_i is the total force exerted by the springs on the node. The total force is given by summing over the springs connected to the ith node:

$$F_i = \sum_{j=1}^{5} -c_{ij}x_i - k\dot{x}_i, \tag{2}$$

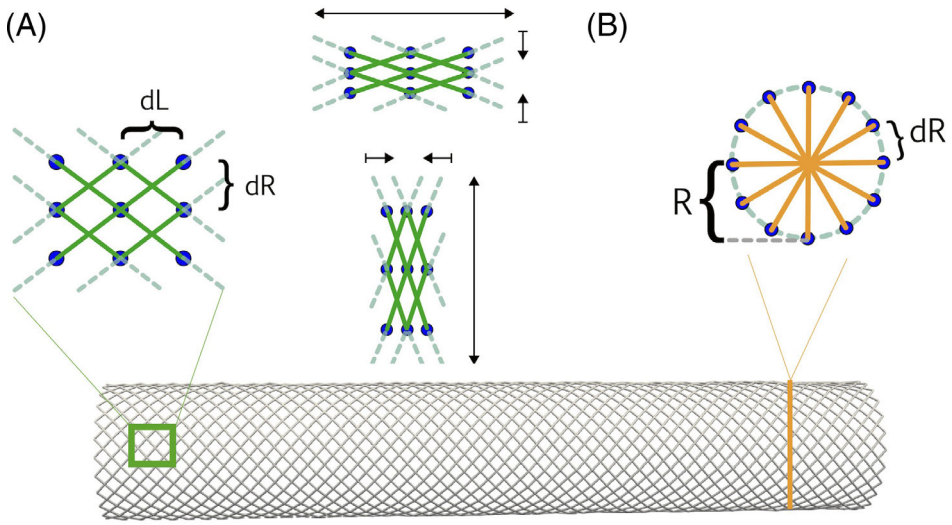

FIGURE 1 Structure of the virtual flow diverter. A, Scissor-like connectivity of the surface spring elements. B, Radial connectivity of the inner spring elements. Note that on the vFD at the bottom only the surface elements (green) are shown, and the inner springs (orange) are not visible

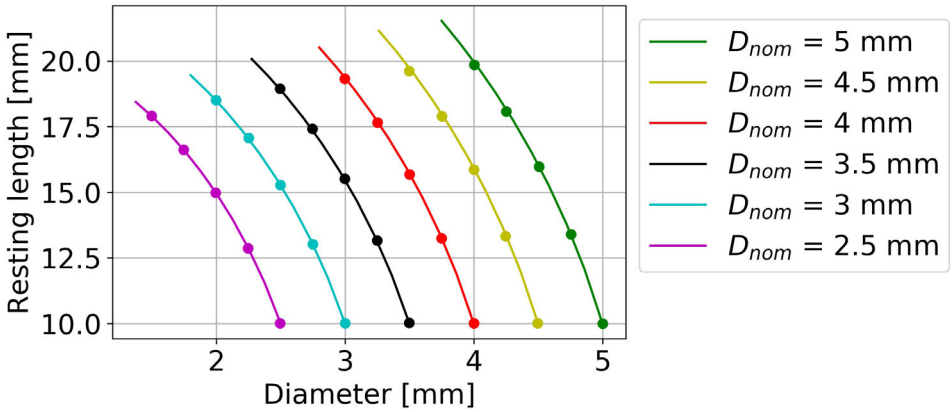

FIGURE 2 Resting length of FDs of various nominal diameters when inserted into different size arteries. The markers show vendor data (same as in Reference [33]), while the continuous lines represent the computed values. Note that resting length for the virtual FDs means that all the surface springs (Figure 1A) are force-free

Nominal diameter (mm)	2.5	3	3.5	4	4.5	5
dL/dR	0.54	0.48	0.44	0.4	0.37	0.35

TABLE 1 Fitted ratio of virtual braid distances (ie, dL/dR) for data shown in Figure 2

where $k = 0.03$ is a small damping coefficient necessary to avoid oscillation (damping ratio $\zeta = 0.047$), and c_{ij} is the spring coefficient corresponding to either the surface type or the inner connection-type springs. The equation of motion is solved using a simple iterative Verlet method. Note that it is possible to simplify the motion equations by neglecting inertial effects completely (ie, quasi-static approximation). This in most cases yields similar results in terms of the final vFD surface position; however, it also produces lower quality meshes. It is especially true near high-curvature regions or vessel surface irregularities, where the lack of inertial effects seems to result in highly non-homogeneous angle and surface shape distribution in the final vFD spring structure. Therefore, for all results in this work the inertial form of the equation of motion was solved.

The vFD motion is constrained by the vessel wall, which is extracted from DSA images using VMTK (version 1.4, www.vmtk.org). The segmented vessel lumen is represented as a triangulated mesh and the centreline of the vessel is stored during the process. The collision between the vFD and the vessel lumen is checked using ray-triangle intersection. To increase the performance of this step, an axis aligned bounding box (AABB) tree is constructed[35] from the triangle set of the vessel lumen at the start of the computations. This tree is then used to strongly reduce the number of surface triangles needed to be checked for collision.

2.1 | Mechanical properties and validations

This vFD model has three parameters for a given FD that describe its mechanical behaviour: the ratio of braid distances (dL/dR) and the two spring coefficients (c_0, c_1). The first one is a geometric feature that dictates the length contraction as discussed above. The two coefficients are derived from a mechanical measurement on real FDs as depicted in Figure 3.

The FD is placed over a 'V′ shaped notch and pressed with a tensile tester machine. The specimen undergoes gradual bending and compression while the displacement of the presser head and the exerted force are recorded. This measurement is replicated numerically with the virtual FD structure, using the same sizes and shapes for both the notch and the presser head. The spring coefficients are set to replicate the arising forces at a given presser-head displacement. The results of this fitting are shown in Figure 4 for two FDs of the same type with different diameters.

Every measurement was repeated three times. Due to the use of fictitious masses, the temporal dynamics of the vFD might not follow the behaviour of the real FD; therefore, all the numerical data points are considered from stationary simulation states. The fitted spring coefficients are listed in Table 2.

2.2 | Comparison with real deployment

One important property of the spring-mass model is that it can replicate crucial parts of the deployment mechanics. In a real deployment scenario, the device is delivered via an endovascular catheter. When the FD reaches the desired

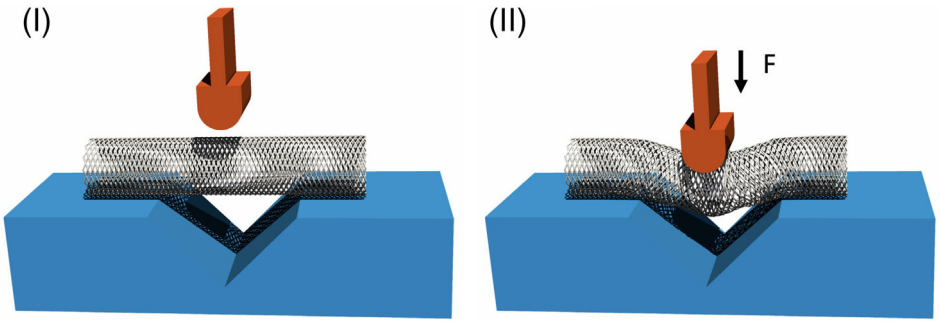

FIGURE 3 Overview rendering of the mechanical measurement. The tested FDs were pressed in a tensile tester machine, and the exerted force vs the displacement of the presser head was recorded

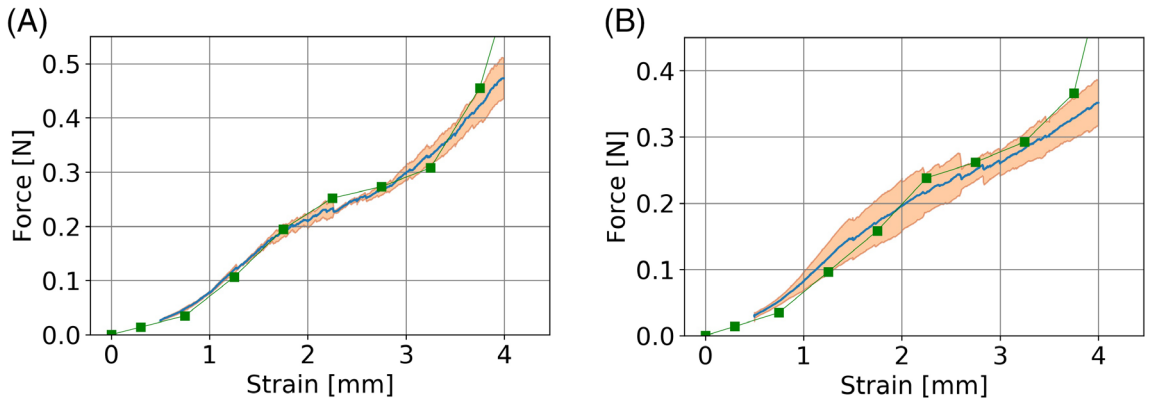

FIGURE 4 Mechanical deformation test of two PED FDs of different diameters. The shaded region denotes the variance of the repeated measurements, and the continuous blue line is their average. The results of the vFDs under the same deformation are shown by green connected markers

TABLE 2 Fitted spring coefficients

Diameter (mm)	4	5
Inner spring coefficient (N/m)	0.1	0.08
Surface spring coefficient (N/m)	0.6	0.4

position, the deployment is done by retracting the microcatheter while simultaneously advancing the insertion wire. The virtually inserted FD is first placed in a compressed state along the centreline of the vessel. It is then gradually opened up from the distal end towards the proximal end, following the velocity of the catheter retraction. Figure 5 depicts three stages of a virtual deployment as the vFD is opens up gradually.

The sequential opening is important to predict the length of the implanted device. The local length of FD segments changes as a function of the local expansion radius (see Figure 2). The expansion radius in turn is affected by local geometric features, such as the local radius of the vessel. Therefore, the modelling of gradual FD opening is important to allow the structure of the FD to adapt to the geometry correctly. Expanding the whole vFD at once can lead to length overestimation or underestimation, depending on the compressed initial length. Furthermore, the parts of the FD that are already expanded and fully in contact with the vessel wall should not move on the vessel surface in an ideal scenario. In our model, the approximation of an infinitely high friction coefficient with the vessel wall was used. The vFD can freely move away from the wall but while there is contact, it cannot slide on it.

The results of a virtual deployment session are compared with a real deployment in a size-accurate 3D printed IA geometry. The advantage of the 3D printed model is that it allows for higher contrast in the CT records, and therefore the position of the implanted FD can be reconstructed with greater accuracy. A Pipeline Flex 4 × 25 mm (48 struts, 75% cobalt chromium and 25% platinum; Medtronic, Plc.) was used. The FD in the 3D printed model was deployed by an experienced medical practitioner (IS) using a Phenom 27 catheter deployment system (Cathera, Inc). Figure 6A shows the final reconstructed surface of the FD inside the 3D printed geometry. Figure 6B shows the results of the corresponding virtual deployment and the distance (ie, the difference) between the surfaces of the FD and vFD.

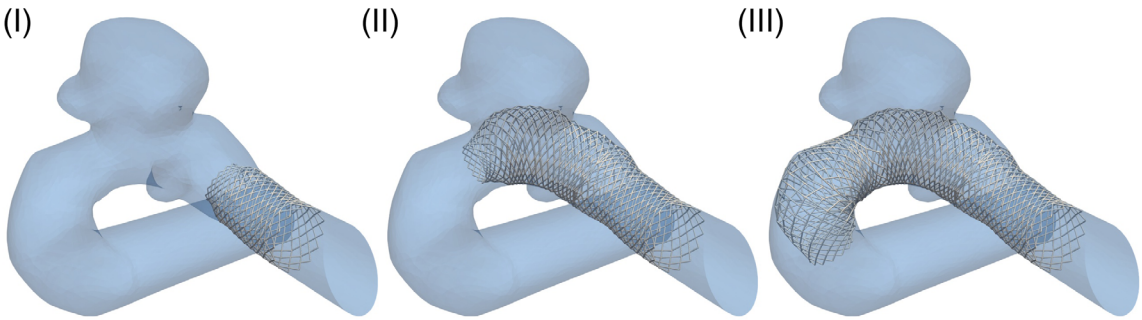

FIGURE 5 From left to right: three steps of the sequential opening of a vFD in front of the aneurysmal neck starting from the distal end. The model replicates the real implantation process

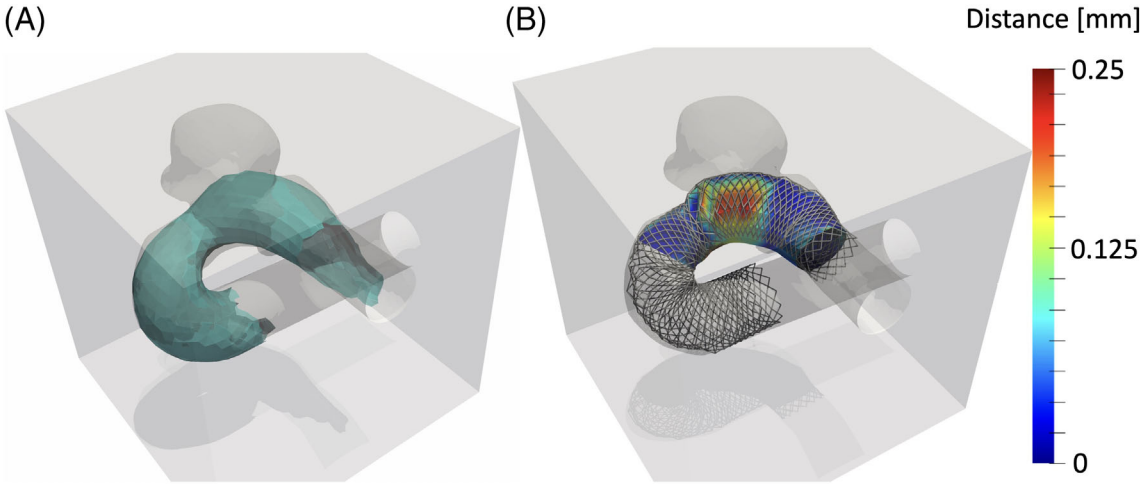

FIGURE 6 A, The segmented surface of the FD inside the 3D printed geometry. B, Virtually deployed vFD showing the distance from the reference FD deployment (Figure 6A) using an overlayed color map

The largest discrepancy, while not too large (around 0.25 mm), arises in front of the aneurysmal neck. The real FD bulges into the sac more than its virtual counterpart. The major reason for this is that the virtual deployment was homogeneous along the whole length of the vFD, while the real implantation followed the usual protocol of trying to increase the surface density in front of the neck. In a real scenario, the medical practitioner can modify the relative motion of the catheter retraction and the insertion wire to locally influence the surface density of the FD (ie, apply 'push-pull'). However, a denser surface through push means longitudinal compression of the FD, which also results in more radial expansion that explains the difference in Figure 6B. This is an important component that is often missing from virtual FD deployment techniques. Since the expansion of our vFD is similar to the real expansion mechanism, it is possible to include longitudinal compression effects. The distance between the spring cross-section units (dL in Figure 1) at the moment of release from the catheter can be set dynamically during the deployment. Decreasing it from the original value mimics the pushing of the insertion wire against the retractive movement of the catheter. This directly leads to local surface compression along the deployment axis (ie, the centreline), while increasing dL leads to local stretching (ie, pull). Note that this does not change the vFD structure itself, it only introduces additional forces during the deployment.

3 | RESULTS

The described vFD model was applied in four different deployment scenarios for quantitative comparison in the same geometry that was used for the surface validation. The first difference between the deployments is the application of push. The second one is the nominal diameter of the vFD, where 4 and 5 mm diameters were used. Figure 7A shows a

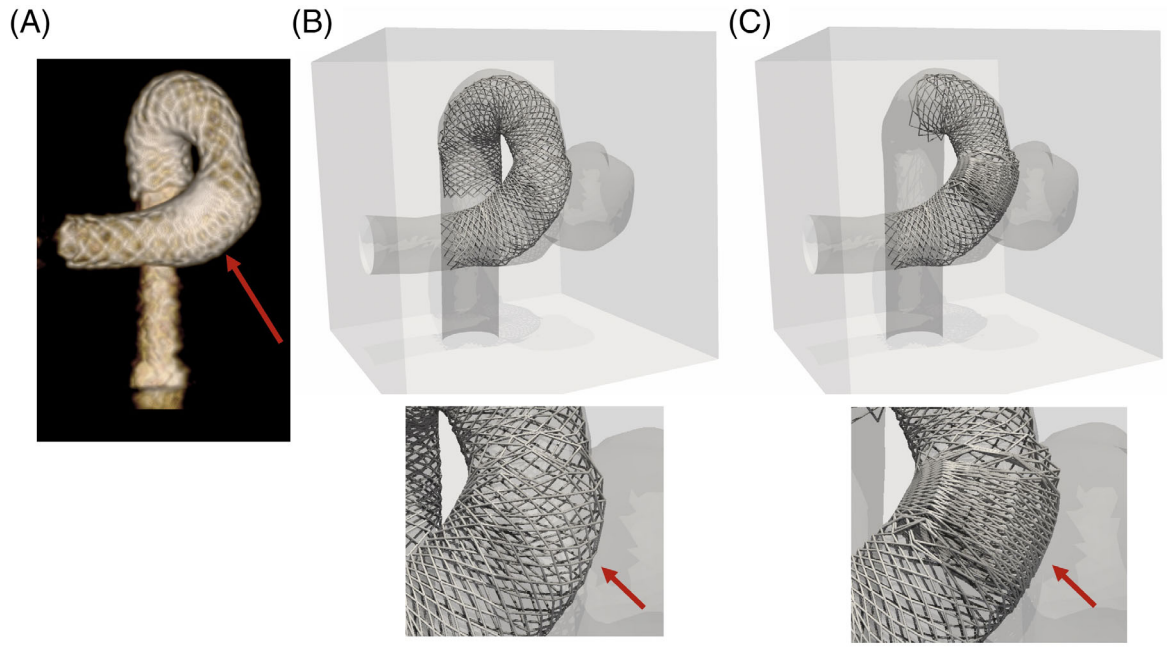

FIGURE 7 A, Overview of the surface density of the real FD. B, vFD without push-pull. C, vFD with the application of push

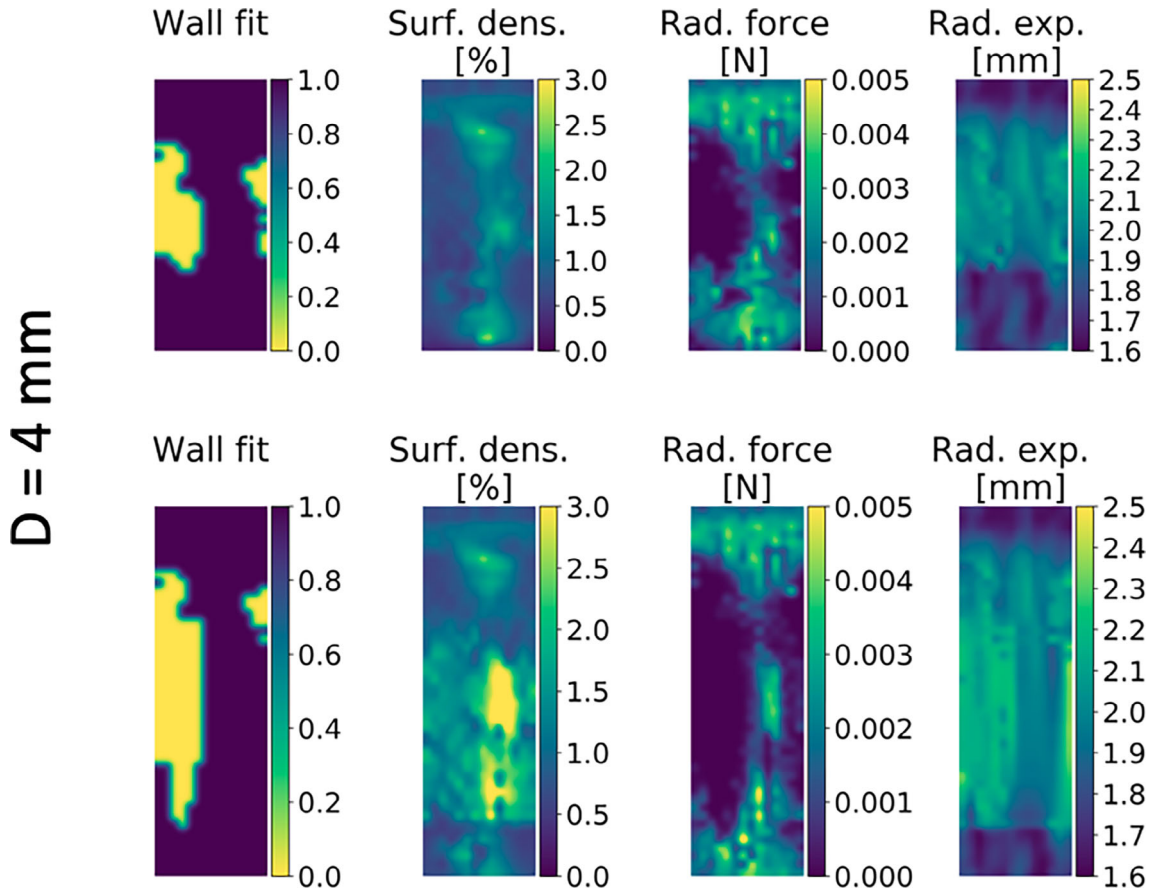

FIGURE 8 Resulting quantities after the virtual deployment projected to the surface of the vFD. (Top row) No push-pull applied. (Bottom row) A push of 66% dL reduction applied at the same location as in Figure 7C

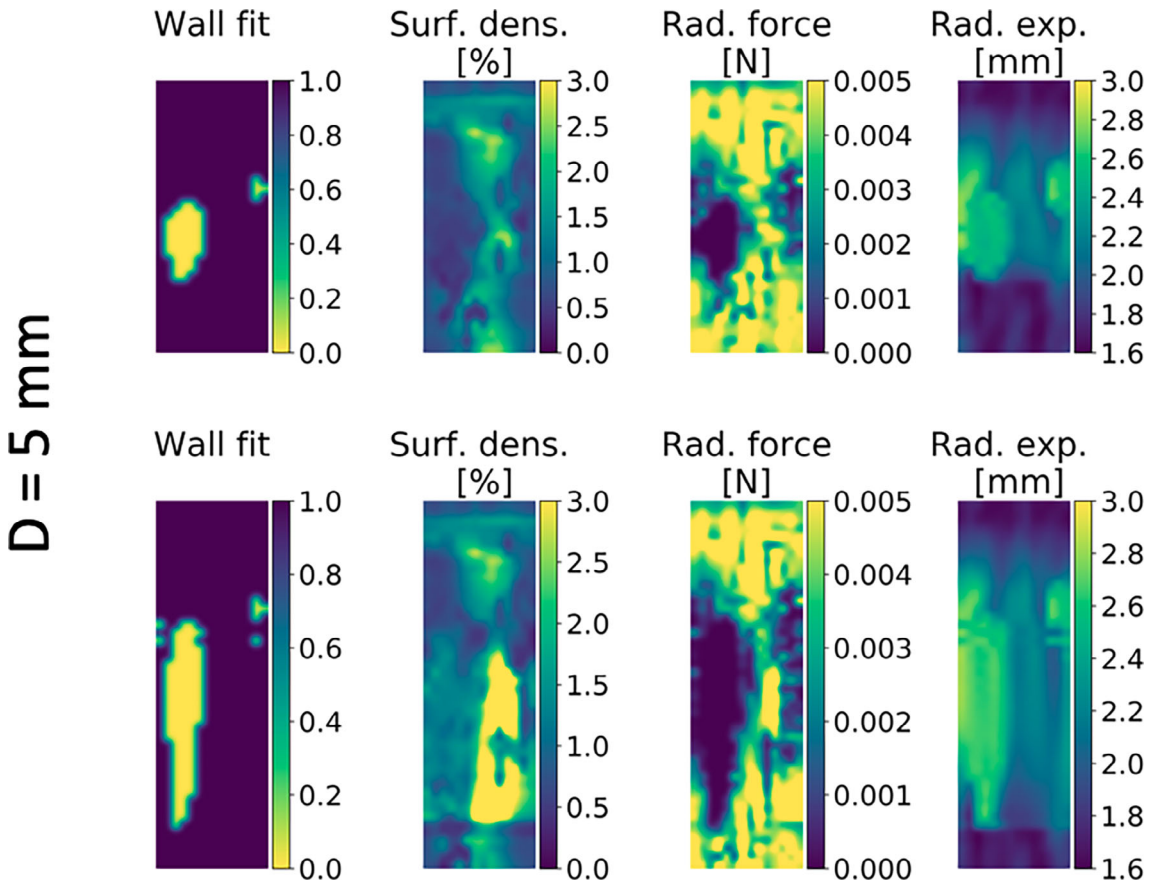

FIGURE 9 Resulting quantities after the virtual deployment projected to the surface of the vFD. (Top row) No push-pull applied. (Bottom row) A push of 66% dL reduction applied at the same location as in Figure 7C. Note that for easier comparison the colour scales are kept the same as in Figure 8 except for the radial expansion

TABLE 3 Comparison of the four investigated cases

Diameter (mm)	Resting length (mm)	Push applied	Avg. dens. inc. across the neck (%)	Implant. length (mm)	Avg. radial expansion at neck (mm)	Avg. contact pressure across the whole FD (mm Hg)
4	20	No	66	21	2	36.9
4	20	Yes	128	15	2.13	42.6
5	20	No	59	22	2.5	86.1
5	20	Yes	118	17	2.64	83.3

recording of the real deployed FD ($D = 4$ mm). The red arrow in the image points to the region where the surface density was increased. The results of a virtual deployment of the same diameter vFD are depicted in Figure 7B,C, without any push-pull and with push, respectively. In the latter case, compression was introduced by reducing dL by 66% locally in front of the IA neck at the moment of the release form the catheter.

The application of push reduced the maximum surface differences between the real and the vFD from 0.25 mm (Figure 6B) to 0.19 mm in this case, due to the increased radial expansion. At the same time, it also decreased the deployed length significantly. To show a quantitative description on the effects of push and the change in diameter, the resulting values were projected to the surface of the vFD. The perianeurysmal region of these surface colourmaps is then unfolded for side-by-side comparison. These results for the virtual PED of $D = 4$ mm are shown in Figure 8.

The top row represents the homogeneous expansion process, while the bottom row represents the application of push. Each column depicts an important quantity projected to the unfolded vFD surface. The first column (wall fit)

shows which part of the surface is in contact with the wall after the deployment. The light yellow region represents the surface in front of the IA neck (ie, no wall contact), while the rest (dark blue) shows a good fit on the wall. The second column depicts the increase of the surface density compared with the surface density of the force-free nominal diameter expansion. The vertical middle region of this plot shows a stripe of higher density. The same area shows full-wall contact in the first column plot and is situated along the inner curve of the vessel, opposite to the aneurysmal side. The reason for the higher density is 2-fold. On the one hand, it is caused by being on the inner curve of the parental vessel, which has higher surface curvature compared with the outer side. On the other hand, the contact with the wall limits the possible expansion compared with the other side, where the vFD can expand into the aneurysmal cavity. The third column shows the radial force exerted by the vFD on the wall after deployment. It has a more homogeneous circumferential distribution compared with the surface density in regions, where there is contact with the wall. It suggests that being on the inner or outer curve does not influence the radial component of the exerted force significantly. Finally, the last column shows the radial expansion, which is the distance from the centre of weight of the corresponding cross-sections. Naturally, the higher expansion values in the region of the neck are expected, since here the vFD is only supported by the vessel wall from one side. When increasing the surface density through the application of push (in the same region as depicted in Figure 7C), the results change slightly. The images in the bottom row of Figure 8 are taller, since they represent the same physical section of the vessel as the top row; however, due to the increased surface density, they correspond to a longer section of the unfolded force-free state of the vFD. The most obvious differences arising with the application of push are higher surface density in front of the neck (but also on the opposite side to the neck) and the higher radial force that now peaks around the neck. With increased longitudinal compression, increasing expansion is also expected (as shown in Figure 2). However, in this case, the diameter of the vessel limits the expansion except towards the sac. Therefore, the compressed deployment protrudes into the cavity more.

The trends in the outcomes are qualitatively similar when using an oversized $D = 5$ mm vFD with push and without any push-pull, as shown in Figure 9. However, deploying the oversized vFD in the current geometry shows some adverse effects. Most importantly, the density increase in front of the aneurysmal neck drops compared with the $D = 4$ mm case. Note that the surface density increase is calculated compared with the own equilibrium surface density of the FD; therefore, this decrease is an additional effect on top of having the same number of braids on a larger radius. At the same time, the force exerted on the vessel wall grows significantly. Table 3 shows the quantitative averages.

The application of push that reduces the local deployment length (dL) by 66% results in approximately twice as high local surface density. The total load on the vessel wall (ie, the radial force) does not change substantially. However, implanting the larger vFD does not lead to higher surface density, but it approximately doubles the load on the wall.

Virtual flow diverter implantation methods in general can display limitations in highly tortuous vessels and in strongly dilated sections. Our method can handle these scenarios well. In Figure 10, the current method was applied to two more such geometries to show that it performs stably in these more complicated cases as well.

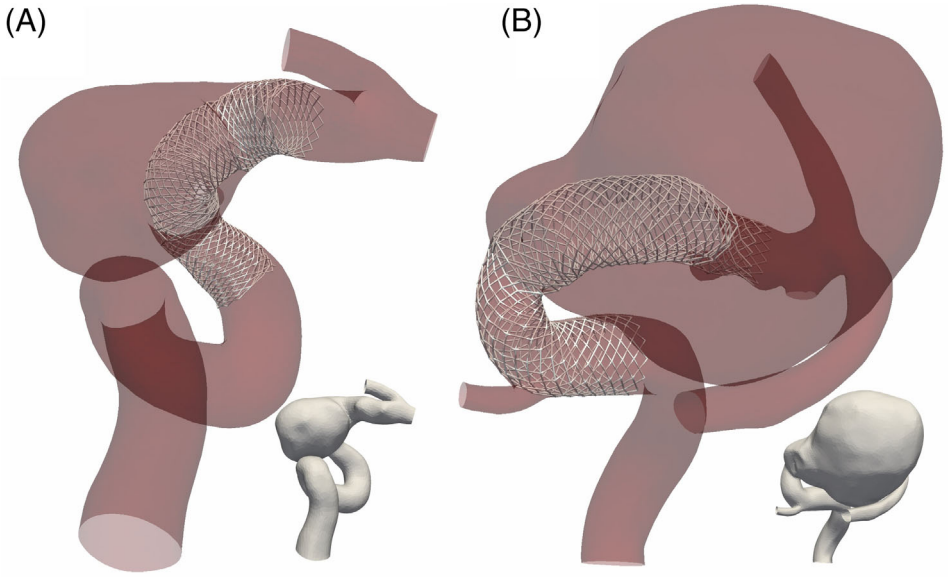

FIGURE 10 Qualitative result on two further IA geometries which are typically difficult to handle numerically. A, The sidewall lesion is located on a parent artery with high tortuosity. B, Giant aneurysm where a large section of the flow diverter is expanded in a space with little or no wall support

4 | DISCUSSION

Flow diversion has been proved to be the most effective endovascular treatment for some types of aneurysms, with a high rate of complete occlusion and low rates of post-operative negative events.[36] However, its application is still associated with potential serious complications, some of which might be possible to avoid by accurate simulation of the mechanical behaviour of the device to be used, called virtual stenting. In the current landscape of virtual FD deployments, a method was needed that can combine several of the important features of existing techniques in one model to allow for more in-depth prediction on the outcomes of the deployment. The advantage of the current method is in the validated mechanical behaviour, high-computational efficiency, small necessary pre-processing effort, fewest possible fit parameters, and the capability to predict the apposition and the mechanical load on the vessel. The performance of our model achieves run-times that fall within the clinically relevant time-scale (order of a few seconds), which allows the exploration of multiple deployment scenarios quickly. This level of performance is unique to models with simplified or surrogate FD representations that do not model the expansion process. However, expansion has high impact on the FD surface location and the wall apposition.[37] It follows naturally that then it is also crucial for making accurate mechanical load predictions. The short- and long-term effects of this load on the parental vessel have not been fully explored yet, but have some implications include vessel straightening and radial dilatation.[38,39] To understand these in more detail in the future, accurate wall load prediction is necessary. The presented model can report the arising contact forces including the effects of push-pull, which can also increase the local radial force of the FD. Push is represented as a decrease and pull as an increase in dL during deployment. While the quantitative comparison of forces with a real deployment would be difficult, the three free parameters of the model are fitted to mechanical test results of real FDs and vendor length contraction data. Note that the vessel wall in our case is rigid, since we lack patient-specific information about the local stiffness of the wall and the surrounding tissue support. Therefore, the contact pressure can be slightly overestimated. In comparison, the contact pressures predicted by our model (Table 3) are in the same range as previous FEA-based model predictions[40] in a similarly sized vessel. Furthermore, the information of contact pressure together with the length change can be important for planning the sizing of the FD. One limitation is that the real-braid structure is not resolved explicitly. This can be circumvented similarly to previous solutions (eg, Larrabide et al[28]), where the geometric description of the braids is attached to the surrogate surface to deform with it. Our aim is to reproduce the flow diverter surface accurately, since this virtual stenting method is integrated with our CFD solution,[41] which uses a porous material description of the FD surface. The last component, the porous flow resistance of various flow diverter types is measured and discussed in Reference [42].

In the current IA case, our computation predicts that oversizing the FD has no beneficial effect on the surface density in front of the neck; however, it approximately doubles the contact pressure on the wall. Applying push in front of the neck can produce superior results in this regard, but then the decreased deployment length must be taken into account. A combined effect of the push and the axial length-dependent radial expansion is that when using this additional compression, the vFD surface can bulge further into the IA cavity.

ACKNOWLEDGEMENTS

The authors would like to thank for the help and support of Eszter Bognár and Péter Nagy with the mechanical tensile test measurements of the FDs. This research was supported by the National Brain Research Program under the contract number 2017-1.2.1-NKP-2017-00002 and by the European Union Horizon 2020 research and innovation programme under grant agreement no. 675451 (CompBioMed project). This work was also supported by the BME-Biotechnology FIKP grant of EMMI (BME FIKP-BIO).

ORCID

Gábor Závodszky https://orcid.org/0000-0003-0150-0229

REFERENCES

1. Chalouhi N, Hoh BL, Hasan D. Review of cerebral aneurysm formation, growth, and rupture. *Stroke*. 2013;44(12):3613-3622.
2. Ropper AH, Zervas NT. Outcome 1 year after SAH from cerebral aneurysm: management morbidity, mortality, and functional status in 112 consecutive good-risk patients. *J Neurosurg*. 1984;60(5):909-915.
3. Kelly P, Stein J, Shafqat S, et al. Functional recovery after rehabilitation for cerebellar stroke. *Stroke*. 2001;32(2):530-534.
4. Vlak MH, Algra A, Brandenburg R, Rinkel GJ. Prevalence of unruptured intracranial aneurysms, with emphasis on sex, age, comorbidity, country, and time period: a systematic review and meta-analysis. *Lancet Neurol*. 2011;10(7):626-636.

5. Berg P, Voß S, Janiga G, et al. Multiple Aneurysms AnaTomy CHallenge 2018 (MATCH)—phase II: rupture risk assessment. *Int J Comput Assist Radiol Surg*. 2019;14(10):1795-1804.
6. Wiebers DO, Torner JC, Meissner I. Impact of unruptured intracranial aneurysms on public health in the United States. *Stroke*. 1992;23 (10):1416-1419.
7. Szikora I, Berentei Z, Kulcsar Z, et al. Treatment of intracranial aneurysms by functional reconstruction of the parent artery: the Budapest experience with the pipeline embolization device. *Am J Neuroradiol*. 2010;31(6):1139-1147.
8. Nelson PK, Lylyk P, Szikora I, Wetzel S, Wanke I, Fiorella D. The pipeline embolization device for the intracranial treatment of aneurysms trial. *Am J Neuroradiol*. 2011;32(1):34-40.
9. John S, Bain MD, Hui FK, et al. Long-term follow-up of in-stent stenosis after pipeline flow diversion treatment of intracranial aneurysms. *Neurosurgery*. 2016;78(6):862-867.
10. Mühl-Benninghaus R, Haußmann A, Simgen A, Tomori T, Reith W, Yilmaz U. Transient in-stent stenosis: a common finding after flow diverter implantation. *J Neurointerv Surg*. 2019;11(2):196-199.
11. Byrne JV, Beltechi R, Yarnold JA, Birks J, Kamran M. Early experience in the treatment of intra-cranial aneurysms by endovascular flow diversion: a multicentre prospective study. *PLoS One*. 2010;5(9):e12492.
12. Siddiqui AH, Abla AA, Kan P, et al. Panacea or problem: flow diverters in the treatment of symptomatic large or giant fusiform vertebrobasilar aneurysms. *J Neurosurg*. 2012;116(6):1258-1266.
13. Alderazi YJ, Shastri D, Kass-Hout T, Prestigiacomo CJ, Gandhi CD. Flow diverters for intracranial aneurysms. *Stroke Research and Treatment*. 2014;2014:1-12.
14. Colby GP, Lin LM, Gomez JF, et al. Immediate procedural outcomes in 35 consecutive pipeline embolization cases: a single-center, single-user experience. *J Neurointerv Surg*. 2013;5(3):237-246.
15. Çinar C, Bozkaya H, Oran İ. Endovascular treatment of cranial aneurysms with the pipeline flow-diverting stent: preliminary mid-term results. *Diagn Interv Radiol*. 2013;19(2):154-164.
16. Lv X, Yang H, Liu P, Li Y. Flow-diverter devices in the treatment of intracranial aneurysms: a meta-analysis and systematic review. *Neuroradiol J*. 2016;29(1):66-71.
17. Heller R, Malek A. Parent vessel size and curvature strongly influence risk of incomplete stent apposition in enterprise intracranial aneurysm stent coiling. *Am J Neuroradiol*. 2011;32(9):1714-1720.
18. Makoyeva A, Bing F, Darsaut T, Salazkin I, Raymond J. The varying porosity of braided self-expanding stents and flow diverters: an experimental study. *Am J Neuroradiol*. 2013;34(3):596-602.
19. Xiang J, Ma D, Snyder KV, Levy EI, Siddiqui AH, Meng H. Increasing flow diversion for cerebral aneurysm treatment using a single flow diverter. *Neurosurgery*. 2014;75(3):286-294.
20. Bouillot P, Brina O, Yilmaz H, et al. Virtual-versus-real implantation of flow diverters: clinical potential and influence of vascular geometry. *Am J Neuroradiol*. 2016;37(11):2079-2086.
21. Damiano RJ, Tutino VM, Paliwal N, et al. Compacting a single flow diverter versus overlapping flow diverters for intracranial aneurysms: a computational study. *Am J Neuroradiol*. 2017;38(3):603-610.
22. Valencia LF, Montagnat J, Orkisz M. 3D models for vascular lumen segmentation in MRA images and for artery-stenting simulation. *IRBM*. 2007;28(2):65-71.
23. Kim M, Taulbee DB, Tremmel M, Meng H. Comparison of two stents in modifying cerebral aneurysm hemodynamics. *Ann Biomed Eng*. 2008;36(5):726-741.
24. Tremmel M, Xiang J, Natarajan SK, et al. Alteration of intraaneurysmal hemodynamics for flow diversion using enterprise and vision stents. *World Neurosurg*. 2010;74(2–3):306-315.
25. Bernardini A, Larrabide I, Petrini L, et al. Deployment of self-expandable stents in aneurysmatic cerebral vessels: comparison of different computational approaches for interventional planning. *Comput Methods Biomech Biomed Eng*. 2012;15(3):303-311.
26. De Bock S, Iannaccone F, De Santis G, et al. Our capricious vessels: the influence of stent design and vessel geometry on the mechanics of intracranial aneurysm stent deployment. *J Biomech*. 2012;45(8):1353-1359.
27. Appanaboyina S, Mut F, Löhner R, Putman C, Cebral J. Simulation of intracranial aneurysm stenting: techniques and challenges. *Comput Methods Appl Mech Eng*. 2009;198(45–46):3567-3582.
28. Larrabide I, Kim M, Augsburger L, Villa-Uriol MC, Rüfenacht D, Frangi AF. Fast virtual deployment of self-expandable stents: method and in vitro evaluation for intracranial aneurysmal stenting. *Med Image Anal*. 2012;16(3):721-730.
29. Paliwal N, Yu H, Xu J, et al. Virtual stenting workflow with vessel-specific initialization and adaptive expansion for neurovascular stents and flow diverters. *Comput Methods Biomech Biomed Engin*. 2016;19(13):1423-1431.
30. Bernardini A, Larrabide I, Morales HG, et al. Influence of different computational approaches for stent deployment on cerebral aneurysm haemodynamics. *Interface Focus*. 2011;1(3):338-348.
31. Spranger K, Ventikos Y. Which spring is the best? Comparison of methods for virtual stenting. *IEEE Trans Biomed Eng*. 2014;61(7):1998-2010.
32. Ma D, Dumont TM, Kosukegawa H, et al. High fidelity virtual stenting (HiFiVS) for intracranial aneurysm flow diversion: in vitro and in silico. *Ann Biomed Eng*. 2013;41(10):2143-2156.
33. Bouillot P, Brina O, Ouared R, et al. Geometrical deployment for braided stent. *Med Image Anal*. 2016;30:85-94.
34. Litwinowicz P, Miller G. Efficient techniques for interactive texture placement. *Proceedings of the 21st Annual Conference on Computer Graphics and Interactive Techniques*. New York, NY: ACM; 1994:119-122.

35. Gvd B. Efficient collision detection of complex deformable models using AABB trees. *J Graphics Tools*. 1997;2(4):1-13.
36. Becske T, Brinjikji W, Potts MB, et al. Long-term clinical and angiographic outcomes following pipeline embolization device treatment of complex internal carotid artery aneurysms: five-year results of the pipeline for uncoilable or failed aneurysms trial. *Neurosurgery*. 2017;80(1):40-48.
37. Ma D, Dargush GF, Natarajan SK, Levy EI, Siddiqui AH, Meng H. Computer modeling of deployment and mechanical expansion of neurovascular flow diverter in patient-specific intracranial aneurysms. *J Biomech*. 2012;45(13):2256-2263.
38. King R, Chueh JY, Van Der Bom I, et al. The effect of intracranial stent implantation on the curvature of the cerebrovasculature. *Am J Neuroradiol*. 2012;33(9):1657-1662.
39. Voß S, Berg P, Janiga G, Skalej M, Beuing O. Variability of intra-aneurysmal hemodynamics caused by stent-induced vessel deformation. *Curr Dir Biomed Eng*. 2017;3(2):305-308.
40. Fu W, Xia Q. Interaction between flow diverter and parent artery of intracranial aneurysm: a computational study. *Appl Bionics Biomech*. 2017;2017:1-9.
41. Závodszky G, Paál G. Validation of a lattice Boltzmann method implementation for a 3D transient fluid flow in an intracranial aneurysm geometry. *Int J Heat Fluid Flow*. 2013;44:276-283.
42. Csippa B, Gyürki D, Závodszky G, Szikora I, Paál G. Hydrodynamic resistance of intracranial flow-diverter stents: measurement description and data evaluation. *Cardiovasc Eng Technol*. 2020;11(1):1-13.

How to cite this article: Závodszky G, Csippa B, Paál G, Szikora I. A novel virtual flow diverter implantation method with realistic deployment mechanics and validated force response. *Int J Numer Meth Biomed Engng*. 2020;36:e3340. https://doi.org/10.1002/cnm.3340